Automated 3D profiler for laser beam characterization

Max Korolev

Bachelorarbeit in Physik
angefertigt im Physikalischen Institut

vorgelegt der
Mathematisch-Naturwissenschaftlichen Fakultät
der
Rheinischen Friedrich-Wilhelms-Universität
Bonn

July 2026

Ich versichere, dass ich diese Arbeit selbstständig verfasst und keine anderen als die angegebenen Quellen und Hilfsmittel benutzt sowie die Zitate kenntlich gemacht habe.

Bonn, 27.07.26 .... Korolev ....

Datum Unterschrift

Gutachter und Betreuer: Prof. Dr. Sebastian Hofferberth
Gutachter: Prof. Dr. Stefan Linden

Acknowledgements

I would like to thank Prof. Dr. Sebastian Hofferberth for giving me the opportunity to write my thesis in this research group. I would also like to thank Prof. Dr. Stefan Linden for kindly agreeing to serve as the second examiner. Furthermore, I would like to thank Daniil, Matthias and Benedikt for their support throughout this project. Finally, I would like to thank the entire NQO Group for creating a welcoming and enjoyable working environment.

Contents

1 Introduction **1**

2 Pinhole beam profiler **3**

2.1 Working principle . . . 3
2.2 Beam profiler setup . . . 3
2.3 Measurement procedure . . . 4
2.3.1 Signal acquisition . . . 4
2.3.2 Beam localization . . . 5
2.3.3 Scan strategy . . . 6
2.3.4 Automatic gain adjustment . . . 8
2.4 Data analysis . . . 10
2.4.1 Signal processing . . . 10
2.4.2 Gaussian beam fitting . . . 10
2.5 Photodetector characterization . . . 12
2.5.1 Linearity . . . 12
2.5.2 Gain calibration . . . 13
2.6 Measurement assumptions and limitations . . . 15

3 Test measurements **20**

3.1 Beam profile measurements . . . 20
3.2 Beam propagation measurements . . . 23
3.3 Comparison with a camera-based beam profiler . . . 28

4 Conclusion and Outlook **30**

A Appendix **32**

A.1 Analytical Evaluation of the Finite Pinhole Effect . . . 32

Bibliography **34**

List of Figures **36**

List of Tables **38**

Used Tools **39**

CHAPTER 1

Introduction

Precise control of the spatial properties of laser beams is a fundamental requirement in many experiments in atomic, molecular and optical physics. In particular, the spatial intensity distribution determines the focal intensity and therefore strongly influences the interaction between laser light and matter [1].

In the Rubidium Quantum Optics (RQO) experiment of the Nonlinear Quantum Optics group, tightly focused laser beams are used in experiments with ultracold atoms [2]. Achieving a high-quality Gaussian beam profile is essential, as even small deviations from an ideal beam can introduce unwanted complexity into the experiment. Accurate beam characterization is therefore a prerequisite for the alignment and optimization of the optical system.

Since the probe beam is focused to a waist below $10\,\mu\text{m}$, reliable beam characterization becomes increasingly challenging. Several techniques exist for measuring the spatial intensity distribution of laser beams, each offering different advantages and limitations. Camera-based beam profilers provide fast two-dimensional measurements of the beam profile. However, their performance is limited by the finite detector pixel size, dynamic range and sensor saturation. These limitations become particularly significant for tightly focused beams, where only a small number of pixels sample the beam and the large intensity gradient near the focus can exceed the sensor's usable range [3].

Knife-edge measurements provide an alternative approach by translating a sharp edge across the beam while recording the transmitted optical power. The beam radius is obtained from the differentiated transmission curve with high accuracy, and by repeating scans in two orthogonal directions at different axial positions, the beam propagation can be characterized. Nevertheless, each measurement yields only one-dimensional information. Recovering the full transverse beam profile requires multiple independent scans and provides only indirect access to the intensity distribution. As a result, localized beam distortions, higher-order modes and other deviations from an ideal Gaussian profile are more difficult to identify than with techniques that directly measure the complete two-dimensional intensity distribution [4].

Scanning aperture profilers overcome these limitations by mechanically scanning a microscopic pinhole across the beam and recording the transmitted optical power. In contrast to camera-based systems, their spatial resolution is determined primarily by the pinhole diameter rather than the detector pixel size, allowing accurate characterization of beam waists of only a few micrometers. At the same time, the complete two-dimensional intensity distribution can be reconstructed, making pinhole profilers particularly well suited for the characterization of tightly focused laser beams [5].

Beam propagation measurements require a sequence of two-dimensional beam profile measurements at many positions along the optical axis. Since each transverse profile is reconstructed point by point by scanning the pinhole across the beam, manually performing such measurements is both time-consuming and prone to positioning errors. Automating the measurement procedure not only reduces the required user intervention but also improves measurement efficiency and reproducibility. For this reason, an automated pinhole-based beam profiler was developed. A motorized three-axis translation stage scans the pinhole across the beam at multiple positions along the optical axis, allowing the beam profile to be reconstructed throughout its propagation. The developed system further incorporates automatic beam localization, adaptive scan windows and automatic gain adjustment of the photodetector system, enabling efficient and reproducible characterization of tightly focused laser beams.

The objective of this bachelor's thesis is the development, implementation and experimental evaluation of the automated beam profiler. Chapter 2 first introduces the operating principle of the profiler before describing its experimental realization, the measurement procedure and the implemented data analysis. The performance of the system is then evaluated in Chapter 3 through a characterization of the photodetector and beam profile measurements, followed by beam propagation measurements that demonstrate the capabilities of the developed profiler.

CHAPTER 2

Pinhole beam profiler

This chapter presents the developed pinhole beam profiler and the methodology used for beam characterization. First, the operating principle of the profiler is introduced. The experimental setup and the automated measurement procedure are then described, followed by the data analysis used to reconstruct the beam profiles and determine the beam parameters. Finally, the photodetector characterization as well as the assumptions and limitations of the measurement method are discussed.

2.1 Working principle

The beam profiler is designed to reconstruct the transverse intensity distribution of a focused laser beam at different positions along its propagation direction.

Rather than imaging the beam directly with a camera, the profiler samples the beam using a microscopic pinhole. At each scan position, the optical power transmitted through the pinhole is collected by a photodetector. By scanning the pinhole across the beam and recording the transmitted optical power at successive positions, the transverse intensity distribution can be reconstructed.

Repeating this procedure at different positions along the optical axis yields a series of transverse beam profiles describing the evolution of the beam during propagation. These measurements provide the basis for the subsequent determination of the characteristic beam parameters.

2.2 Beam profiler setup

Figure 2.1 shows a schematic overview of the developed beam profiler. The system consists of an optical subsystem for beam scanning and an electronic subsystem for signal acquisition and detector control.

The optical subsystem is built around a motorized three-axis translation stage (Newport VP-25XA-XYZR). A 1 µm pinhole and a photodetector (Thorlabs PDAPC2) are mounted on the translation stage such that their relative position remains fixed during scanning. The photodetector is positioned directly behind the pinhole to ensure that essentially all optical power transmitted through the aperture is detected. The x- and y-axes of the translation stage are used to scan the pinhole across the beam, while the z-axis allows measurements at different positions along the propagation direction. The translation stage is driven by three motion controllers (Newport SMC100CC), which are controlled from a PC using a custom Python script.

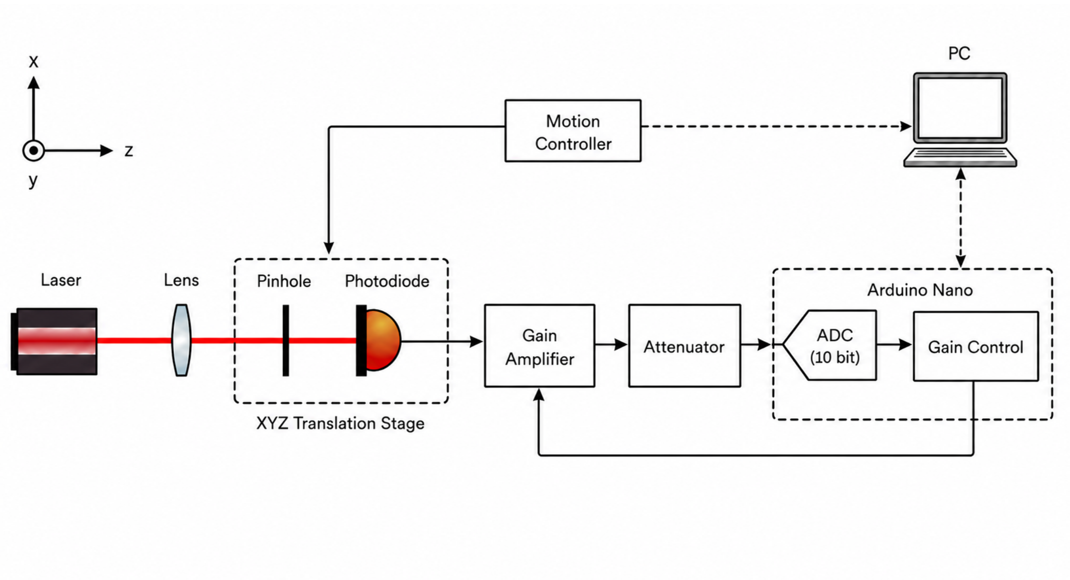

Figure 2.1: Schematic overview of the beam profiler. The laser beam is focused onto a pinhole mounted on a motorized translation stage. The transmitted optical power is detected by a photodetector, digitized by an Arduino Nano and processed by the measurement software running on a PC. The photodiode and gain amplifier shown in the figure are integrated in the photodetector.

The laser beam is focused onto the pinhole using a focusing lens. The focusing lens is positioned such that the beam waist is located close to the center of the translation stage travel range. This allows measurements to be performed symmetrically around the beam waist in all three spatial directions.

The electronic subsystem consists of an Arduino Nano, which serves as the interface between the photodetector and the measurement software running on the PC. The analog output voltage of the photodetector is digitized by the Arduino's integrated 10-bit analog-to-digital converter (ADC) and transmitted to the PC via a USB serial connection. In addition, the Arduino controls the gain setting of the photodetector through one of its digital output pins.

The photodetector output voltage can reach approximately 10 V, exceeding the maximum permissible input voltage of 5 V for the Arduino ADC. Therefore, an 8 dB attenuator is inserted between the photodetector and the Arduino. This reduces the maximum detector output voltage to approximately 4 V, preventing saturation of the ADC input while utilizing most of its available dynamic range.

Together, the optical and electronic subsystems enable automated acquisition of two-dimensional beam profiles at different positions along the propagation axis.

2.3 Measurement procedure

2.3.1 Signal acquisition

The analog output voltage of the photodetector is digitized by the 10-bit ADC of the Arduino, which converts input voltages between 0 V and 5 V into integer values ranging from 0 to 1023. The digitized signal is then transmitted to the PC, where it is processed by the measurement software.

To reduce the influence of random electronic noise, the detector signal is not determined from a single

ADC conversion. Instead, the software acquires 100 consecutive ADC samples at every measurement position and calculates their arithmetic mean. The averaged ADC value is subsequently converted into the corresponding detector voltage U using

$$U = \overline{A}\frac{U_{\mathrm{ref}}}{1023}, \tag{2.1}$$

where $\overline{A}$ is the mean ADC value and $U_{\mathrm{ref}} = 5\,\mathrm{V}$ is the ADC reference voltage.

The number of samples was chosen as a compromise between measurement precision and signal acquisition time. Increasing the number of samples N further would reduce the statistical uncertainty of the averaged detector signal. However, this improvement scales only with $1/\sqrt{N}$, whereas the signal acquisition time increases approximately linearly with the number of acquired samples. Consequently, increasing the number of samples beyond 100 provides only a limited improvement in measurement precision while substantially increasing the overall measurement time.

The statistical uncertainty of each measurement point is quantified by the standard error of the mean (SEM),

$$\sigma_{\overline{\mathrm{A}}} = \frac{\sigma_{\mathrm{A}}}{\sqrt{N}}, \tag{2.2}$$

where σ_{A} is the standard deviation of the recorded ADC values.

For each measurement point, the software stores both the averaged detector voltage and its corresponding SEM. Unlike the standard deviation, which describes the spread of the individual ADC samples, the SEM quantifies the uncertainty of the averaged detector voltage. These uncertainties are propagated throughout the subsequent data analysis.

Before the measurement sequence, a dark measurement is performed with the laser beam blocked. For each available detector gain setting, the detector voltage is acquired repeatedly, allowing the mean dark voltage and its statistical uncertainty to be determined. The measured dark signal is assumed to be primarily determined by the electronic offset and noise of the photodetector, amplifier and data acquisition electronics, while the contribution from ambient light transmitted through the 1 µm pinhole is negligible under the experimental conditions.

Since the electronic offset depends primarily on the selected detector gain rather than on the position of the translation stage, the dark measurement is performed only once before the complete beam propagation measurement. Repeating the dark measurement before every transverse scan would require blocking the laser at each axial position, interrupting the automated measurement process and substantially increasing the overall measurement time. The experimentally determined dark voltages and their corresponding statistical uncertainties are stored and subsequently subtracted during the signal preprocessing described in Section 2.4.

2.3.2 Beam localization

Before a beam profile measurement is performed, the beam waist is localized automatically. Following a manual coarse alignment, which places the beam within the vicinity of the pinhole, the localization algorithm determines the beam waist position. This position serves as the center of the subsequent axial scan, allowing the beam propagation to be measured approximately symmetrically about the focus.

The manual coarse alignment considerably reduces the search space, since locating a beam with a radius of only a few micrometers within the 25 mm travel range of the translation stage by exhaustive scanning would require an impractically large number of measurement points and thereby excessive measurement time.

Since the transmitted optical power is maximal when the pinhole is centered on the beam, the beam waist can be localized by maximizing the detector signal. The implemented localization algorithm combines coordinate-wise hill climbing [6] with parabolic interpolation [7]. As the search approaches the beam maximum, the step size is reduced adaptively to improve the localization accuracy. Because hill climbing performs a local optimization, the initial position must already lie within the vicinity of the beam center, which is ensured by the preceding manual coarse alignment.

Starting from the manually determined initial position, the beam waist is located iteratively by maximizing the detector signal along the x-, y-, and z-axes in succession. For the currently optimized axis, the signal is measured at the current position and at two neighboring positions separated by the current step size h. At each position, the detector signal is obtained by averaging 100 consecutive ADC samples, as described in Section 2.3.1 to reduce the influence of random electronic noise.

If either neighboring position yields a signal exceeding the current value by more than a predefined relative threshold, the translation stage is moved to that position and the optimization continues. The threshold prevents unnecessary stage movements caused by statistical fluctuations.

Otherwise, a quadratic function is fitted to the three measured points. The position of the local maximum is estimated from the vertex of the interpolating parabola [8]

$$\Delta = \frac{h}{2}\frac{S_{-} - S_{+}}{S_{-} - 2S_0 + S_{+}}, \tag{2.3}$$

where S_{-}, S_0, and S_{+} denote the measured signals at the positions $x - h$, x, and $x + h$, respectively.

The interpolation is performed only if

$$S_{-} - 2S_0 + S_{+} < 0, \tag{2.4}$$

ensuring that the fitted parabola is concave and therefore possesses a local maximum. Furthermore, the estimated displacement is constrained to lie within the interval $[x - h, x + h]$ to avoid extrapolation beyond the measured points. The interpolated position is accepted only if an additional measurement confirms that the detector signal has increased. By estimating the maximum between adjacent sampling points, the interpolation provides sub-step localization without requiring a further reduction of the step size.

If the interpolation does not improve the solution, the step size is reduced by a factor of two and the optimization is repeated. The algorithm terminates once the predefined minimum step size has been reached along all three axes without further improvement of the detector signal. The final stage position is taken as the beam waist position.

The beam localization algorithm is illustrated in Figure 2.2.

2.3.3 Scan strategy

After the beam waist has been localized, transverse beam profiles are recorded at different positions along the optical axis. At each axial position, the pinhole is translated through the transverse plane according to a predefined scan pattern while the detector signal is acquired. The resulting measurements form the raw data for the subsequent beam analysis.

At each measurement position, the translation stage moves the pinhole to the target coordinates.

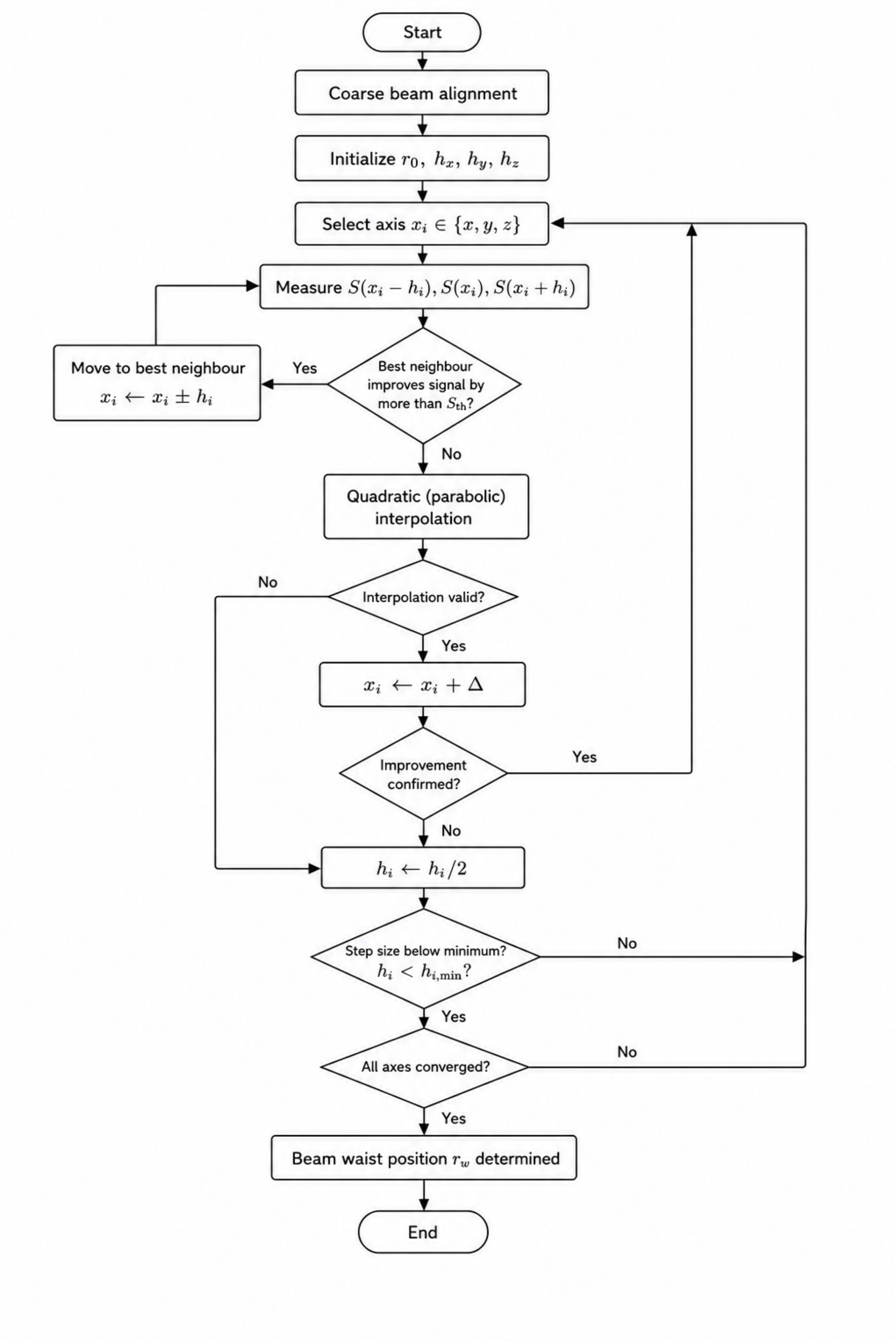

Figure 2.2: Flow chart of the implemented beam localization algorithm. Here, $\mathbf{r}_0$ is the initial stage position, h_i the current step size along axis i, $S(x_\text{i})$ the measured detector signal at position x_i, S_th the predefined relative threshold, Δ the displacement predicted by the parabolic interpolation and $\mathbf{r}_\text{w}$ the estimated beam waist position.

After each movement, a short settling time of 0.4 s is introduced before the detector signal is acquired. This ensures that the detector output has reached a stable value before the measurement is performed. Shorter settling times were found experimentally to result in erroneous measurements, indicating that the detector signal had not fully settled. For every measurement point, the software stores the stage coordinates (x, y, z), the averaged detector voltage, the selected detector gain and the corresponding statistical uncertainty.

Since the beam radius increases with propagation distance from the beam waist, the scan area required to capture the complete beam profile also increases. A scan window chosen too small crops the beam profile and leads to inaccurate beam parameters, whereas a window sufficiently large for all axial positions results in many unnecessary measurements. Consequently, using a fixed scan window for all measurement planes is inefficient.

To overcome this limitation, a center-out square spiral scan with an adaptive stopping criterion is implemented (Figure 2.3). Starting from the beam center, the translation stage moves the pinhole along a square spiral trajectory, extending the scan ring by ring towards larger radial distances. This scan pattern allows the stopping criterion to be evaluated after each completed spiral ring without interrupting the scan sequence. The measurement can therefore be terminated as soon as the outer scan region no longer contains significant beam signal, avoiding unnecessary measurements while requiring only minimal additional stage movement.

After each completed spiral ring, the maximum detector signal within the current ring, $S_{\text{ring,max}}$, is compared with the maximum detector signal measured during the entire scan, S_{max}. The corresponding relative edge signal is defined as

$$R_{\text{max}} = \frac{S_{\text{ring,max}}}{S_{\text{max}}}. \tag{2.5}$$

If R_{max} falls below a predefined threshold for two consecutive spiral rings, the remaining scan area is assumed to contain no significant beam signal and the scan is terminated automatically. Otherwise, the measurement continues with the next spiral ring. The threshold is defined by the user prior to the measurement and should be selected according to the expected beam characteristics and the desired measurement sensitivity. The requirement of two consecutive rings reduces the likelihood of premature termination due to isolated low-signal measurements.

After each transverse scan, the measurement position corresponding to the maximum recorded detector signal is used as the center of the subsequent transverse scan. Since the beam center may shift slightly along the propagation direction due to residual optical misalignment or beam tilt, this continuously updates the scan center and ensures that the beam remains within the measurement region without requiring repeated beam localization.

2.3.4 Automatic gain adjustment

During a beam profile measurement, the optical power transmitted through the pinhole spans several orders of magnitude. For an ideal Gaussian beam, the transmitted power is highest near the beam center and decreases exponentially towards the beam edges. In practice, optical aberrations may additionally produce weak halos or ring-like intensity distributions surrounding the main beam. Although these features contain only a small fraction of the total optical power, they are important for assessing the beam quality. Using a single fixed detector gain therefore requires the amplification to be chosen such that the intense beam center neither saturates the photodetector nor exceeds the input range of the ADC. As a

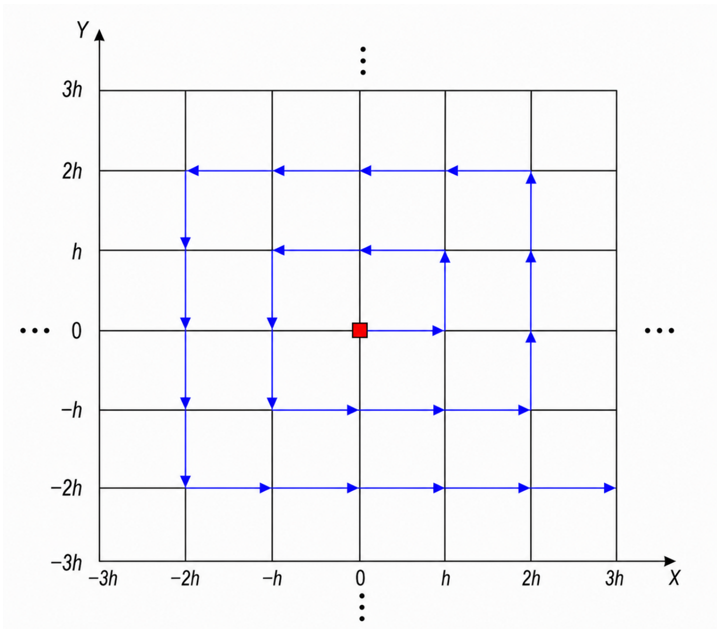

Figure 2.3: Schematic illustration of the adaptive square spiral scan. Starting from the current scan center, which initially coincides with the localized beam waist, the pinhole is translated along a square spiral trajectory with constant step size h. After each completed spiral ring, the maximum detector signal within the current ring is evaluated. The scan terminates after two consecutive rings whose maximum signal falls below the predefined stopping threshold. The red square indicates the current scan center.

result, much weaker detector signals occupy only a small fraction of the available ADC range, resulting in poor effective resolution and potentially becoming indistinguishable from the detector noise.

To overcome this limitation, the detector gain is adjusted automatically throughout the measurement. The photodetector provides eight discrete gain settings ranging from 0 dB to 70 dB in steps of 10 dB, corresponding to an overall amplification range of approximately three orders of magnitude. Each gain increment increases the detector output voltage by approximately a factor of $\sqrt{10} \approx 3.16$.

The gain is adjusted independently for every measurement point. After the detector voltage has been acquired, it is compared with two predefined operating thresholds. If the measured voltage exceeds the upper threshold, the gain is decreased by one step. Conversely, if the voltage falls below the lower threshold, the gain is increased by one step. After each gain adjustment, the detector voltage is measured again using the new gain setting. This procedure is repeated until the detector voltage lies within the desired operating range.

Rather than resolving the entire detector dynamic range with a single gain setting, the available ADC resolution is effectively utilized within each gain range. As a result, weak detector signals can be recorded with nearly the same effective digital resolution as the intense beam center, substantially extending the measurable dynamic range without requiring a higher-resolution ADC.

The operating thresholds and gain calibration factors are determined experimentally from the photodetector characterization presented in Chapter 2.5. These values are subsequently used throughout the beam profile measurements.

2.4 Data analysis

The measurement procedure described in the previous sections yields detector voltages recorded at different spatial positions and detector gain settings. These raw data do not directly represent the beam intensity distribution and therefore require preprocessing steps before the beam parameters can be determined.

First, the measured voltages are corrected for the gain-dependent dark offset and normalized with respect to the detector gain. The resulting detector signals are then assigned to their corresponding spatial coordinates to reconstruct the two-dimensional beam profile at each axial position. Finally, two-dimensional Gaussian functions are fitted to the reconstructed beam profiles, allowing the characteristic beam parameters to be extracted from their evolution along the propagation direction.

2.4.1 Signal processing

The raw detector voltages cannot be compared directly because they are acquired at different detector gain settings and contain an electronic offset originating from the photodetector and the data acquisition electronics. Therefore, the measured voltages are corrected before reconstructing the beam profiles.

For each measurement point, the gain-dependent dark voltage U_{dark} is subtracted from the measured detector voltage U_{meas}, yielding the corrected detector voltage U_{corr},

$$U_{\text{corr}} = U_{\text{meas}} - U_{\text{dark}}. \tag{2.6}$$

The uncertainty of the corrected detector voltage is calculated by Gaussian error propagation using the uncertainties of the measured detector voltage and the corresponding dark voltage.

Subsequently, the corrected detector voltages are normalized to a common reference gain using the experimentally determined gain calibration factors. For a detector operated at gain setting G, the normalized detector voltage U_{norm} is given by

$$U_{\text{norm}} = \frac{U_{\text{corr}}}{G_{\text{rel}}(G)}, \tag{2.7}$$

where $G_{\text{rel}}(G)$ denotes the cumulative amplification relative to the reference gain obtained from the detector gain calibration. The uncertainty of the normalized detector voltage is calculated analogously by Gaussian error propagation, taking into account the uncertainties of both the corrected detector voltage and the gain calibration factor.

The normalized detector voltages and their associated uncertainties constitute the input data for all subsequent beam profile analyses.

2.4.2 Gaussian beam fitting

After signal preprocessing, the corrected detector signals are assigned to their corresponding measurement coordinates, yielding a two-dimensional beam profile for each axial position.

The beam profiler is intended for the characterization of laser beams operating in the fundamental transverse electromagnetic mode TEM_{00}. Within the paraxial approximation, the transverse intensity distribution is described by a Gaussian function [9]. Therefore, each measured beam profile is evaluated by fitting a two-dimensional Gaussian function to the reconstructed beam profile.

$$I(x,y) = I_0 \exp\left[-2\left(\frac{(x-x_0)^2}{w_\mathrm{x}^2} + \frac{(y-y_0)^2}{w_\mathrm{y}^2}\right)\right] + I_\mathrm{off}, \tag{2.8}$$

The fit parameters are the peak intensity I_0, the beam center (x_0, y_0), the $1/e^2$ beam radii w_x and w_y and the constant background offset I_off.

The constant offset I_off is included although a dark correction has already been applied. It accounts for residual systematic offsets that remain after dark correction.

The model is fitted to the measured intensity distribution using a weighted nonlinear least-squares fit, where the propagated statistical uncertainties of the detector signal are used as weighting factors. The covariance matrix returned by the weighted least-squares fit provides the statistical uncertainties of the fitted beam parameters. In addition, systematic uncertainties arising from the manufacturer's specified positioning accuracy of the translation stage and from the uncertainty of the photodetector gain calibration are propagated numerically by varying the corresponding input quantities within their uncertainties and repeating the Gaussian fit. The individual systematic contributions are then combined in quadrature.

Furthermore, to assess how well the Gaussian fit describes the measured profile, the coefficient of determination R^2 is calculated for every fitted transverse beam profile. It is defined as [10]

$$R^2 = 1 - \frac{\sum_{i=1}^{N} \left(I_i - I_{\mathrm{fit},i}\right)^2}{\sum_{i=1}^{N} \left(I_i - \overline{I}\right)^2}. \tag{2.9}$$

where I_i denotes the measured detector signal, $I_\mathrm{fit,i}$ the corresponding fitted intensity and $\overline{I}$ the mean measured intensity. The coefficient of determination quantifies how well the Gaussian model describes the measured beam profile. Values close to unity indicate an excellent agreement, whereas smaller values reveal deviations from an ideal Gaussian profile caused, for example by optical aberrations.

The beam radii obtained from the individual two-dimensional Gaussian fits are evaluated as functions of the axial position. The propagation is analyzed independently for the horizontal and vertical beam radii.

For a Gaussian beam, the evolution of the beam radius along the propagation direction is described by [9]

$$w(z) = w_0 \sqrt{1 + \left(\frac{z - z_0}{z_\mathrm{R}}\right)^2}, \tag{2.10}$$

where w_0 denotes the beam waist radius, z_0 the beam waist position and z_R the Rayleigh length. The Rayleigh length corresponds to the propagation distance from the beam waist at which the beam radius has increased to

$$w(z_0 \pm z_\mathrm{R}) = \sqrt{2}\, w_0. \tag{2.11}$$

The measured beam radii $w_{\mathrm{x}(z)}$ and $w_{\mathrm{y}(z)}$ are fitted independently using this propagation model. The propagation fit is performed as a weighted nonlinear least-square fit, where the uncertainties of the beam radii obtained from the two-dimensional Gaussian fits are used as weighting factors. The statistical uncertainties of the beam radii obtained from the two-dimensional Gaussian fits are used as weighting factors for the propagation fit. Systematic uncertainties arising from the translation stage calibration and the gain calibration are propagated numerically to the fitted propagation parameters.

Besides the beam waist and the Rayleigh length, the beam quality factor M^2 is determined. For a Gaussian beam, the Rayleigh length is related to the beam waist by [11]

$$z_R = \frac{\pi w_0^2}{M^2 \lambda} \tag{2.12}$$

where λ is the laser wavelength. Therefore, the beam quality factor can be calculated from the fitted beam parameters according to

$$M^2 = \frac{\pi w_0^2}{\lambda z_R}. \tag{2.13}$$

The beam quality factor is evaluated independently for the horizontal and vertical directions. An ideal Gaussian beam is characterized by $M^2 = 1$, whereas values larger than 1 indicate an increased divergence compared to an ideal Gaussian beam.

2.5 Photodetector characterization

The automatic gain adjustment described in Section 2.3.4 requires a characterization of the photodetector. In particular, the detector must operate within its linear response range, and the effective gain associated with each gain setting must be known in order to combine measurements recorded at different gain levels. The photodetector was therefore characterized with respect to its linearity and gain calibration.

2.5.1 Linearity

To determine the linear operating range of the photodetector, the laser beam was directed onto the detector without the pinhole used during beam profile measurements. The incident optical power was varied and measured using an optical power meter, while the corresponding detector output voltage was recorded simultaneously with an oscilloscope. For each measurement point, the detector voltage was calculated as the arithmetic mean of all recorded oscilloscope samples.

Prior to the measurement series, a background measurement was performed with the laser beam blocked to determine the detector offset voltage. The measured background was subsequently subtracted from all recorded voltages before further analysis.

The objective of the linearity characterization was to determine the range of detector output voltages over which the photodetector exhibits a linear response. Since accurate beam profile measurements require operation within this region, the results were used to define the switching thresholds for the automatic gain adjustment described in Section 2.3.4. Because the profiler acquires the detector signal after the 8 dB attenuator, the experimentally determined detector output voltages were converted to the corresponding attenuated voltages before being implemented in the measurement software. The corresponding ADC input voltage was calculated according to

$$V_{\mathrm{ADC}} = V_{\mathrm{det}} \cdot 10^{-8/20}, \tag{2.14}$$

where V_{det} is the photodetector output voltage before attenuation.

To determine the linear operating range, a weighted orthogonal distance regression was performed, taking the uncertainties of both the optical power and the detector voltage into account. Since both measured quantities are affected by experimental uncertainties, orthogonal distance regression was preferred over ordinary least-squares regression. The fitting range was selected by visual inspection to include only the region exhibiting an approximately linear detector response. The resulting linear model served as a reference for evaluating the detector response over the entire measurement range. The measured detector response together with the fitted linear model is shown in Figure 2.4.

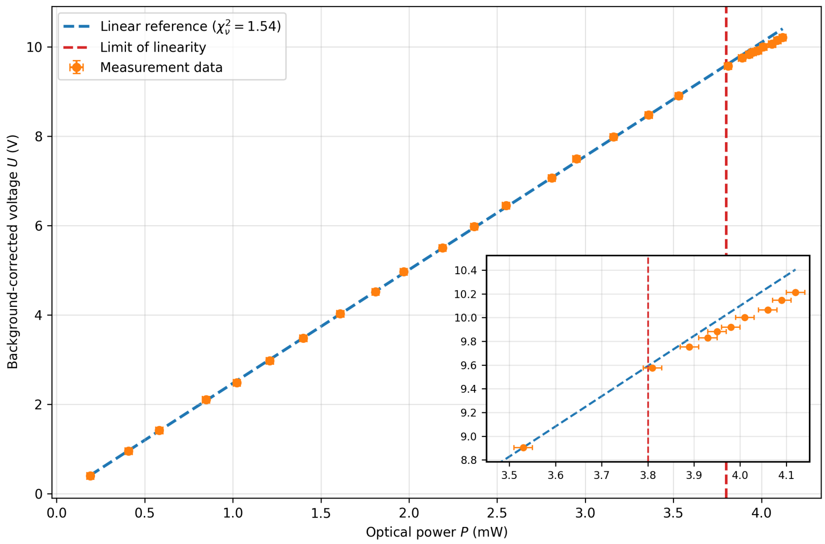

Figure 2.4: Measured detector output voltage as a function of optical power. The dashed blue line represents the weighted orthogonal distance regression performed within the linear operating range. The dashed red line indicates the upper limit of the linear operating region adopted for the automatic gain adjustment. The inset shows the onset of detector saturation at high optical powers.

The detector response agrees closely with the fitted linear model over most of the investigated range. The regression yields a reduced chi-squared value of $\chi^2_\nu = 1.54$, indicating good agreement between the model and the measurement data within the experimental uncertainties. The upper limit of the linear operating range was conservatively defined as a detector output voltage of 9.6 V, corresponding to approximately 3.8 V after the 8 dB attenuator. This value was adopted as the upper switching threshold for the automatic gain adjustment.

The lower switching threshold was set to 3 V after the attenuator. This value provides sufficient hysteresis relative to the upper threshold to prevent unnecessary gain switching caused by small signal fluctuations while still utilizing a large fraction of the ADC input range.

2.5.2 Gain calibration

Although the photodetector provides nominal gain settings in increments of 10 dB, the corresponding amplification factors must be determined experimentally before measurements acquired at different gain settings can be combined on a common intensity scale. The gain calibration therefore determines the relative amplification between adjacent gain settings.

The calibration was performed using the complete signal acquisition chain employed by the beam profiler, consisting of the photodetector, the attenuator and the Arduino ADC. Consequently, the obtained calibration factors directly correspond to the detector signals processed during beam profile measurements.

As in the linearity measurement, a background measurement was first recorded with the laser beam blocked and subsequently subtracted from all measurements. For each pair of adjacent gain settings, the detector voltage was measured at several optical power levels within the previously determined linear operating range. Using multiple power levels allows the consistency of the gain ratio to be verified while reducing the influence of measurement noise.

Rather than determining the absolute gain of each detector setting, only the relative amplification between adjacent gain settings was measured. Since the detector voltage was measured at identical optical power for both gain settings, the gain factor can be obtained directly from the ratio of the background-corrected detector voltages,

$$A_i = \frac{V_{G+10}}{V_G},$$

where V_G and V_{G+10} denote the detector voltages measured at the gain settings G and $G + 10\,\mathrm{dB}$, respectively. The amplification factor for each gain step was obtained as the arithmetic mean of the voltage ratios measured at the individual optical power levels.

For an ideal detector, a gain increment of 10 dB corresponds to a voltage amplification of

$$A_{\mathrm{ideal}} = 10^{10/20} = \sqrt{10} \approx 3.16.$$

The cumulative amplification relative to the 0 dB setting was obtained by multiplying the individual gain factors,

$$G_n = \prod_{i=1}^{n} A_i.$$

Assuming independent uncertainties of the individual gain ratios, the uncertainty of the cumulative amplification was calculated using Gaussian error propagation. The cumulative amplification was subsequently converted into decibels according to

$$g_{\mathrm{eff}} = 20\log_{10}(G_n),$$

allowing a direct comparison with the nominal detector gain settings.

The measured amplification factors for the individual 10 dB gain steps are shown in Figure 2.5. For comparison, the ideal amplification factor of $10^{10/20} \approx 3.16$ is indicated by the dashed line. The measured gain factors range from approximately 3.23 to 3.43 and are consistently larger than the nominal value. While the first four gain steps deviate from the ideal value by only 2-4%, the amplification increases more noticeably for the highest gain settings.

Since the gain factors accumulate over successive gain steps, even small deviations of the individual amplification factors lead to an increasing offset between the nominal and the effective detector gain. The resulting cumulative effective gain is shown in Figure 2.6. The measured effective gain agrees closely with the nominal detector settings at low gains but increasingly exceeds the nominal values for higher gain settings, reaching (72.70 ± 0.44) dB at the nominal 70 dB setting.

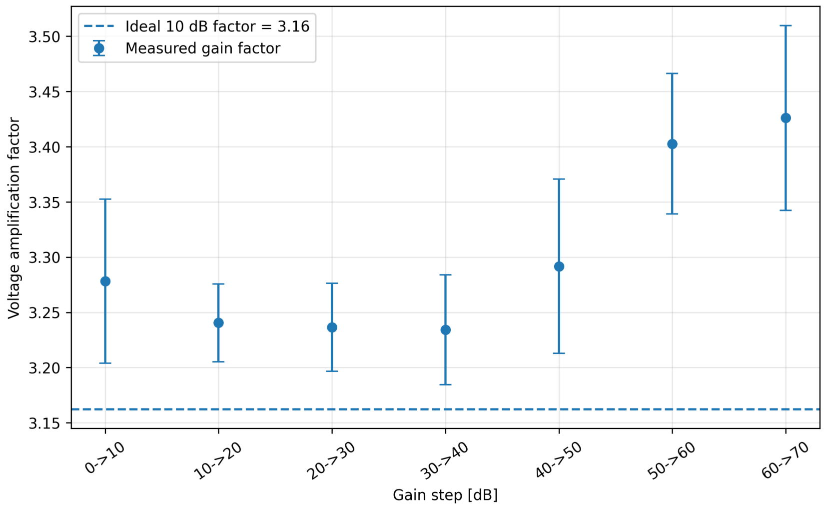

Figure 2.5: Experimentally determined voltage amplification factors for the individual 10 dB gain steps. The dashed line indicates the ideal amplification factor of $10^{10/20} \approx 3.16$. Error bars represent the propagated uncertainties of the measured amplification factors.

The experimentally determined effective gain values are summarized in Table 2.1. These calibrated gain values, together with their associated uncertainties, were subsequently used to normalize all beam profile measurements to the common reference gain of 0 dB. The corresponding calibration uncertainties were propagated together with the statistical detector uncertainties throughout the subsequent data analysis and were included in the uncertainty estimates of the fitted parameters.

Nominal gain (dB)	Effective gain (dB)
10	10.31 ± 0.20
20	20.53 ± 0.22
30	30.73 ± 0.24
40	40.92 ± 0.28
50	51.27 ± 0.35
60	61.91 ± 0.38
70	72.60 ± 0.44

Table 2.1: Experimentally determined effective detector gain relative to the nominal gain settings.

2.6 Measurement assumptions and limitations

In Section 2.1, the detector signal was assumed to be proportional to the local beam intensity, which is valid only for an infinitesimally small pinhole. For a finite pinhole, however, the detector measures the optical power transmitted through the aperture. Throughout the following analysis, the pinhole is modeled as an ideal circular aperture of diameter d. Manufacturing tolerances and the finite thickness of the pinhole are neglected, such that the transmitted optical power is determined solely by the aperture

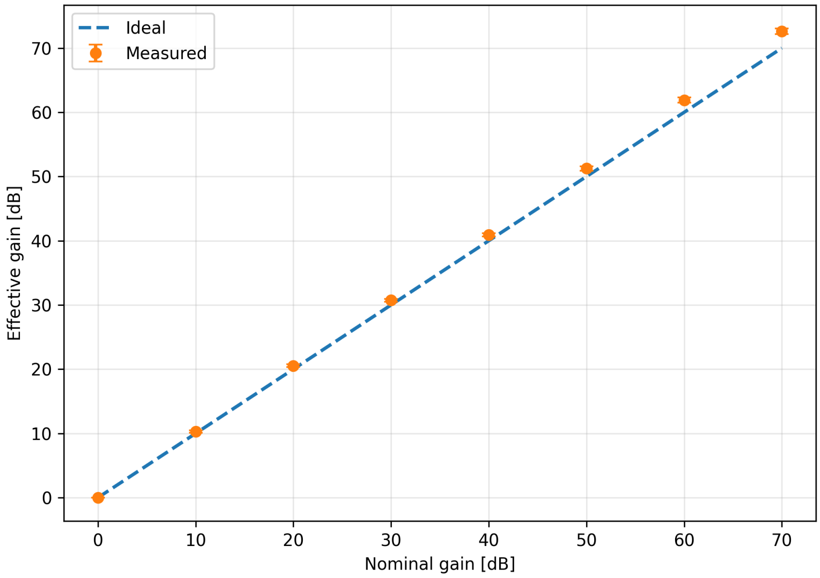

Figure 2.6: Experimentally determined cumulative effective detector gain relative to the nominal gain settings. The dashed line indicates the ideal detector gain.

opening.

Since only the spatial variation of the detector response is relevant for beam characterization, the aperture function is normalized to unit integral. The detector response at each scan position (x_0, y_0) is therefore described by the convolution of the beam intensity distribution $I(x, y)$ with the aperture function $A(x, y)$ [12]

$$S(x_0, y_0) = \iint I(x, y)\, A(x - x_0, y - y_0)\, \mathrm{d}x\, \mathrm{d}y \tag{2.15}$$

where $S(x_0, y_0)$ denotes the normalized detector response. For an ideal circular aperture,

$$A(x, y) = \begin{cases} \dfrac{1}{\pi (d/2)^2}, & x^2 + y^2 \le \left(\dfrac{d}{2}\right)^2 \\ 0, & \text{otherwise} \end{cases} \tag{2.16}$$

such that

$$\iint A(x, y)\, \mathrm{d}x\, \mathrm{d}y = 1. \tag{2.17}$$

The convolution represents the local spatial average of the beam intensity over the aperture area. In the limiting case of an infinitesimally small aperture, the aperture function approaches the two-dimensional Dirac delta function,

$$A(x, y) \longrightarrow \delta(x, y) \tag{2.18}$$

the detector response reduces to

$$S(x, y) = I(x, y), \tag{2.19}$$

which corresponds to the approximation introduced in Section 2.1.

Figure 2.7 illustrates the effect qualitatively for the intentionally exaggerated case of $w/d = 0.75$. Compared with the original Gaussian beam, the measured profile is broadened owing to spatial averaging over the aperture. This example highlights the convolution effect and does not represent the normal operating conditions of the beam profiler.

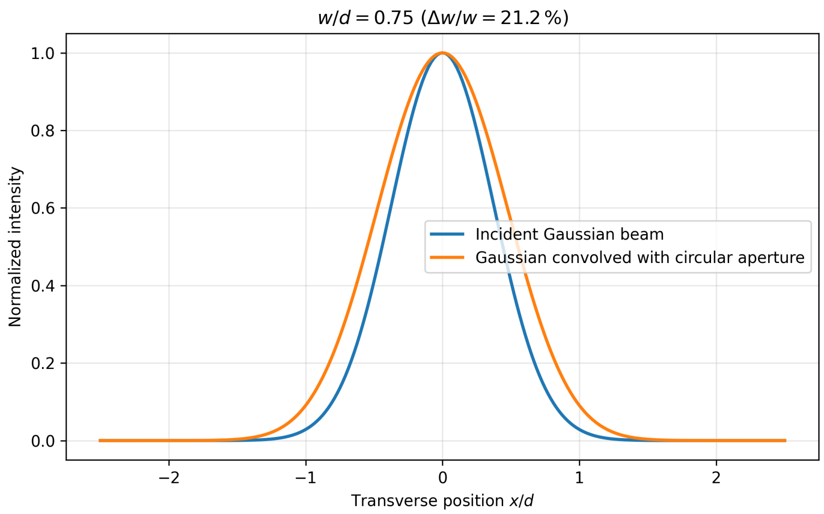

Figure 2.7: Illustration of aperture-induced broadening for a Gaussian beam with $w/d = 0.75$. The example is intentionally chosen to emphasize the convolution effect and does not represent the operating conditions of the beam profiler.

To quantify the influence of the finite aperture on the measured beam radius, the relative beam-radius error was derived analytically as a function of the beam-radius-to-aperture ratio w/d (Appendix A.1) and verified by numerical two-dimensional convolution. For both the analytical derivation and the numerical validation, the incident beam was assumed to be an ideal Gaussian beam. Figure 2.8 shows that the aperture-induced error decreases rapidly with increasing w/d. The numerical results closely follow the analytical prediction over the entire investigated range, demonstrating excellent agreement between both approaches. Representative values are summarized in Table 2.2.

The analysis shows that the finite aperture introduces a predictable systematic broadening of the measured beam profile whose magnitude depends only on w/d. For beam-radius-to-aperture ratios exceeding approximately $w/d = 5$, the aperture-induced broadening remains below 0.5 %. Within the intended operating range of the beam profiler, this effect is sufficiently small that numerical deconvolution would provide little practical benefit.

Although the aperture-induced broadening is small under typical operating conditions, it is instructive to consider whether the original beam intensity could, in principle, be recovered by numerical deconvolution. Applying the Fourier transform to the convolution and using the convolution theorem gives [13]

$$\hat{S}(f_x, f_y) = \hat{I}(f_x, f_y)\, \hat{A}(f_x, f_y), \tag{2.20}$$

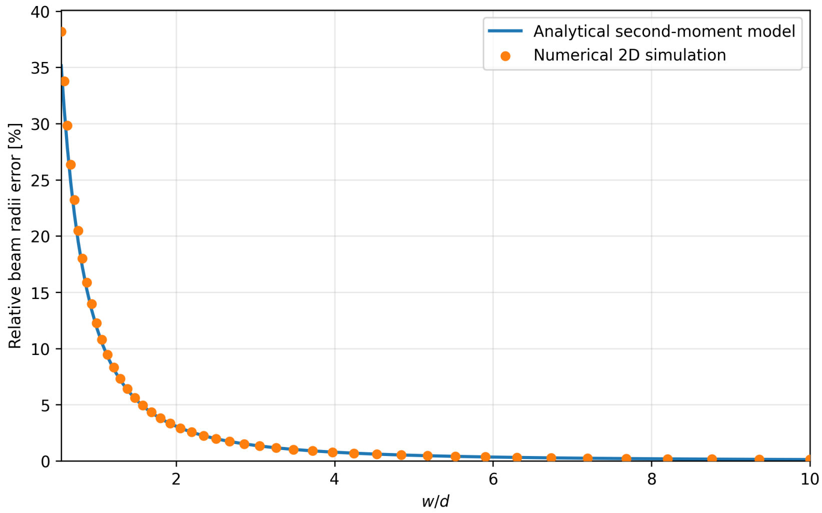

Figure 2.8: Relative beam-radius error for an ideal Gaussian beam caused by aperture convolution as a function of the beam-radius-to-aperture ratio w/d. The numerical results closely follow the analytical prediction over the investigated range.

w/d	Numerical Error (%)	Analytical Error (%)
1	12.126	11.803
2	3.080	3.078
3	1.373	1.379
4	0.773	0.778
5	0.495	0.499
7	0.253	0.255
10	0.124	0.125

Table 2.2: Representative values of the relative beam-radius error caused by aperture convolution for different beam-radius-to-aperture ratios. Analytical and numerical results are listed for comparison.

where hats denote Fourier-transformed quantities. Formally, recovering the incident beam intensity requires

$$\hat{I}(f_x, f_y) = \frac{\hat{S}(f_x, f_y)}{\hat{A}(f_x, f_y)}. \tag{2.21}$$

For the normalized circular aperture [14]

$$\hat{A}(\rho) = \frac{2J_1(\pi d\rho)}{\pi d\rho}, \tag{2.22}$$

where J_1 denotes the first-order Bessel function of the first kind and $\rho = \sqrt{f_x^2 + f_y^2}$ is the radial spatial frequency. Since this jinc-shaped transfer function contains zeros and regions of small magnitude, direct inversion strongly amplifies measurement noise. Although regularization techniques can improve numerical stability, they introduce additional assumptions and may distort the reconstructed intensity distribution. Given the small aperture-induced broadening under normal operating conditions, the expected improvement does not justify the additional computational complexity. Consequently, no deconvolution is applied.

While the convolution model accurately describes spatial averaging by the finite aperture, it neglects diffraction at the pinhole edges. Every finite aperture acts as a diffracting element, producing a characteristic diffraction angle of approximately [15]

$$\theta \approx 1.22\frac{\lambda}{d}, \tag{2.23}$$

where λ denotes the optical wavelength.

The detector is assumed to be positioned immediately behind the pinhole and to possess a sufficiently large active area to collect essentially all transmitted optical power. Under these conditions, diffraction only redistributes the transmitted optical field without changing the detected power. Since all beam profiles are normalized before Gaussian fitting, diffraction behind the pinhole does not influence the extracted beam waist, beam center, Rayleigh length, or beam quality factor. Any remaining wavelength dependence of the measurement system is therefore determined solely by the spectral responsivity of the photodetector.

CHAPTER 3

Test measurements

In this chapter, the performance of the developed beam profiler is evaluated. The evaluation focuses on three aspects. First, the ability of the system to reconstruct transverse beam profiles is assessed using two focusing lenses with different focal lengths. Subsequently, beam propagation measurements are analyzed to determine the beam waist, Rayleigh length and beam quality factor. Finally, the obtained propagation parameters are compared with measurements performed using a camera-based beam profiler to assess the accuracy of the developed system.

3.1 Beam profile measurements

The first step in evaluating the developed beam profiler is to assess its ability to reconstruct the transverse intensity distribution of tightly focused laser beams. For this purpose, beam profiles were recorded close to the beam waist, where the smallest beam radii are expected, using focusing lenses with focal lengths of 100 mm and 50 mm. These configurations produce beam waists that differ by approximately a factor of two and therefore provide a first assessment of the reconstruction performance over a broad range of beam sizes. All measurements were performed at a laser wavelength of 780 nm.

The measurement parameters used for both configurations are summarized in Table 3.1.

Parameter	100 mm lens	50 mm lens
Transverse step size	2 μm	1 μm
Axial step size (near waist)	20 μm	5 μm
Axial step size (outside waist)	60 μm	20 μm
Axial measurement range	$\approx 4\, z_R$	$\approx 5\, z_R$

Table 3.1: Measurement parameters used for the transverse beam-profile measurements.

100 mm focusing lens

Figure 3.1 shows the reconstructed beam profile measured close to the beam waist using the 100 mm focusing lens. The normalized intensity distribution is well described by the fitted two-dimensional

Gaussian model, resulting in a coefficient of determination of $R^2 = 0.9982$. No pronounced higher-order transverse modes or significant deviations from a Gaussian profile are observed.

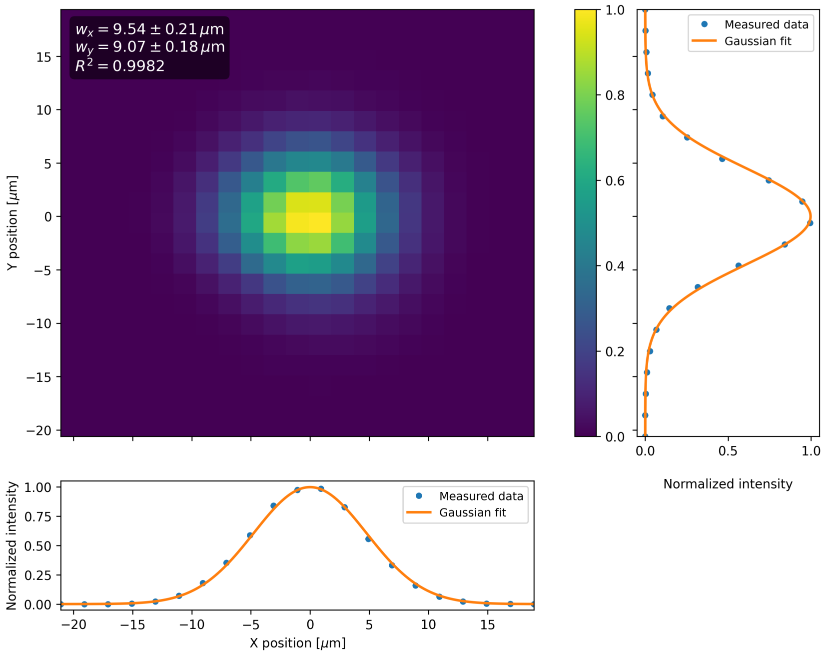

Figure 3.1: Reconstructed beam profile measured close to the beam waist using a 100 mm focusing lens. The left panel shows the normalized two-dimensional intensity distribution. The right and bottom panels display the corresponding vertical and horizontal cross sections through the fitted beam center. The solid lines represent the fitted Gaussian model.

The fitted beam radii are

$$w_x = (9.54 \pm 0.21)\,\mu\text{m}, \tag{3.1}$$
$$w_y = (9.07 \pm 0.18)\,\mu\text{m}. \tag{3.2}$$

The horizontal beam radius exceeds the vertical radius by approximately 5 %, indicating a slight ellipticity of the focused beam. This asymmetry suggests residual optical misalignment or weak astigmatism rather than an artifact of the reconstruction procedure.

A small discontinuity is visible close to the beam maximum. Since its position coincides with the transition between adjacent detector gain settings, it is consistent with residual inaccuracies in the gain calibration. Nevertheless, the measured data remain well described by the Gaussian model, indicating that the observed offset has only a negligible influence on the fitted beam profile.

50 mm focusing lens

The reconstructed beam profile obtained using the 50 mm focusing lens is shown in Figure 3.2. Despite the substantially smaller beam waist, the measured intensity distribution is again well described by the two-dimensional Gaussian model, yielding $R^2 = 0.9947$.

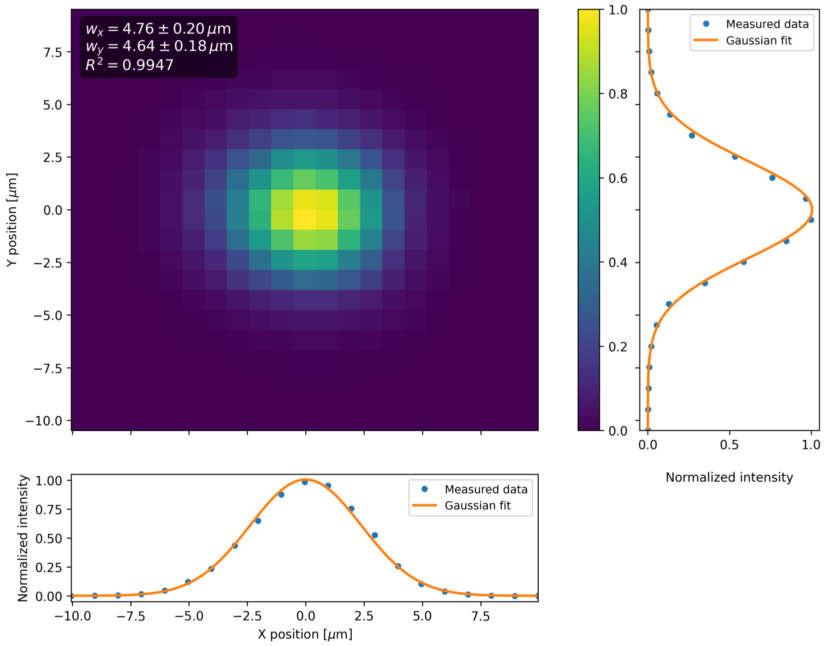

Figure 3.2: Reconstructed beam profile measured close to the beam waist using a 50 mm focusing lens. The left panel shows the normalized two-dimensional intensity distribution. The right and bottom panels display the corresponding vertical and horizontal cross sections through the fitted beam center. The solid lines represent the fitted Gaussian model.

The fitted beam radii are

$$w_x = (4.76 \pm 0.20)\,\mu\mathrm{m}, \tag{3.3}$$
$$w_y = (4.64 \pm 0.18)\,\mu\mathrm{m}. \tag{3.4}$$

Compared with the measurement performed using the 100 mm focusing lens, the beam waist is approximately reduced by a factor of two, as expected from the shorter focal length of the focusing lens. The horizontal and vertical beam radii differ by only approximately 3 %, indicating an almost circular beam profile.

As in the previous measurement, a small discontinuity is observed near the beam maximum owing to the transition between adjacent detector gain settings. Its influence on the fitted beam parameters is again expected to be negligible.

Taken together, the measurements performed with both focusing lenses demonstrate reliable beam-profile reconstruction over a wide range of beam radii. In both cases, the reconstructed intensity distributions are well described by a two-dimensional Gaussian model, yielding coefficients of determination exceeding 0.99. This indicates that the measured beam profiles closely resemble the fundamental Gaussian mode within the measurement uncertainty.

The reconstructed beam waists scale as expected with the focal length of the focusing lens, while the slight ellipticity observed for both measurements suggests that the remaining asymmetry originates primarily from the optical system rather than from the reconstruction algorithm itself. Small discontinuities at the detector gain transition points indicate that the gain calibration could be refined further. While these discontinuities remain consistent with the Gaussian model and have only a negligible influence on the extracted beam parameters, future investigations could compare the current adaptive gain strategy with measurements performed at a fixed detector gain for each transverse scan. Such an approach may improve the smoothness of the reconstructed beam profiles for nearly ideal Gaussian beams, whereas adaptive gain switching remains advantageous when characterizing beams containing weak halos or higher-order intensity structures with a large dynamic range.

Overall, these results demonstrate that the developed beam profiler consistently reconstructs transverse intensity distributions suitable for subsequent Gaussian beam analysis and beam propagation measurements.

3.2 Beam propagation measurements

While the previous section focused on beam profiles at individual axial positions, a complete characterization of a Gaussian beam additionally requires its evolution along the propagation direction.

For this purpose, beam profiles were recorded at multiple axial positions around the beam waist for both focusing lenses. The beam radii extracted from the two-dimensional Gaussian fits were subsequently fitted using the Gaussian beam propagation model introduced in Section 2.4.2. This procedure yields the beam waist radius w, the waist position z_0, the Rayleigh length z_R and the beam quality factor M^2.

Compared with the transverse beam profile measurements, beam propagation measurements require complete two-dimensional scans at many axial positions and are therefore considerably more time-consuming. Using the 100 mm focusing lens, 54 beam profiles were recorded, resulting in a total measurement time of approximately 13 h. For the 50 mm focusing lens, 62 beam profiles were acquired, requiring approximately 21 h.

The measurement time varies considerably along the propagation direction, since the adaptive scan window automatically increases with the beam diameter. For the 50 mm focusing lens, a scan recorded close to the beam waist required approximately 8 min, whereas the final scan at the largest beam diameter took nearly 1 h. This adaptive measurement strategy enables the beam to be sampled over a large propagation range while maintaining adequate spatial resolution and avoiding truncation of the beam profile. Using a fixed scan window would either lead to cropped beam profiles at large beam diameters or require substantially longer acquisition times if the largest scan area were used throughout the entire measurement.

The increasing acquisition time for large beam radii highlights the trade-off between spatial resolution and measurement time that is inherent to point-by-point beam profiling. For applications involving large beam radii, the overall acquisition time can be reduced by choosing measurement parameters appropriate for the required accuracy, for example by employing a larger pinhole diameter or a coarser sampling grid. Such adjustments are generally acceptable when the objective is the determination of global beam parameters rather than the investigation of fine spatial features.

100 mm focusing lens

Representative reconstructed beam profiles measured at different propagation distances are shown in Figure 3.3. As expected for a Gaussian beam, the beam diameter continuously decreases towards the focal plane, reaches its minimum at the beam waist and subsequently diverges again. The adaptive scan window automatically adjusts to the varying beam diameter, allowing the complete transverse intensity distribution to be recorded over the entire propagation range without truncation.

Throughout the propagation, a slight ellipticity of the beam is visible. The beam becomes nearly circular in the vicinity of the beam waist, whereas the ellipticity increases again on either side of the focus. Furthermore, the orientation of the major beam axis changes after passing through the beam waist. This behavior is consistent with weak astigmatism, where the beam waists in the two transverse directions are located at slightly different axial positions. The beam propagation analysis presented below confirms this interpretation quantitatively.

Figure 3.4 shows the extracted beam radii together with the fitted Gaussian beam propagation model. Overall, the measured beam radii are well described by the Gaussian beam propagation model. The corresponding propagation parameters obtained from the Gaussian beam fits are summarized in Table 3.2.

Parameter	100 mm lens	50 mm lens
$w_{0,x}$ [µm]	9.54 ± 0.22	4.79 ± 0.23
$w_{0,y}$ [µm]	9.13 ± 0.19	4.59 ± 0.20
$z_{R,x}$ [mm]	0.3628 ± 0.0046	0.0936 ± 0.0032
$z_{R,y}$ [mm]	0.3248 ± 0.0035	0.0863 ± 0.0027
M_x^2	1.010 ± 0.033	0.988 ± 0.061
M_y^2	1.033 ± 0.032	0.984 ± 0.056
Astigmatism Δz_0 [µm]	58.9 ± 0.1	10.0 ± 0.1

Table 3.2: Beam propagation parameters obtained from the Gaussian beam fits.

Small systematic deviations from the fitted propagation curve are visible, particularly in the y direction, where the measured beam radii tend to lie below the fitted model before the beam waist and above it afterwards. Rather than resulting from random measurement noise, this behavior suggests a slight deviation from ideal Gaussian beam propagation. A likely explanation is the presence of spherical aberration in the focusing optics, which is not accounted for by the Gaussian beam model used for the fit. The fitted waist positions differ by approximately 59 µm, confirming the weak astigmatism already apparent in the reconstructed beam profiles.

The fitted beam quality factors are close to the lower physical limit of $M^2 = 1$. Although the nominal values are physically permissible, their close proximity to unity and the associated uncertainties suggest that they should be interpreted with caution rather than as an unambiguous confirmation of ideal diffraction-limited propagation.

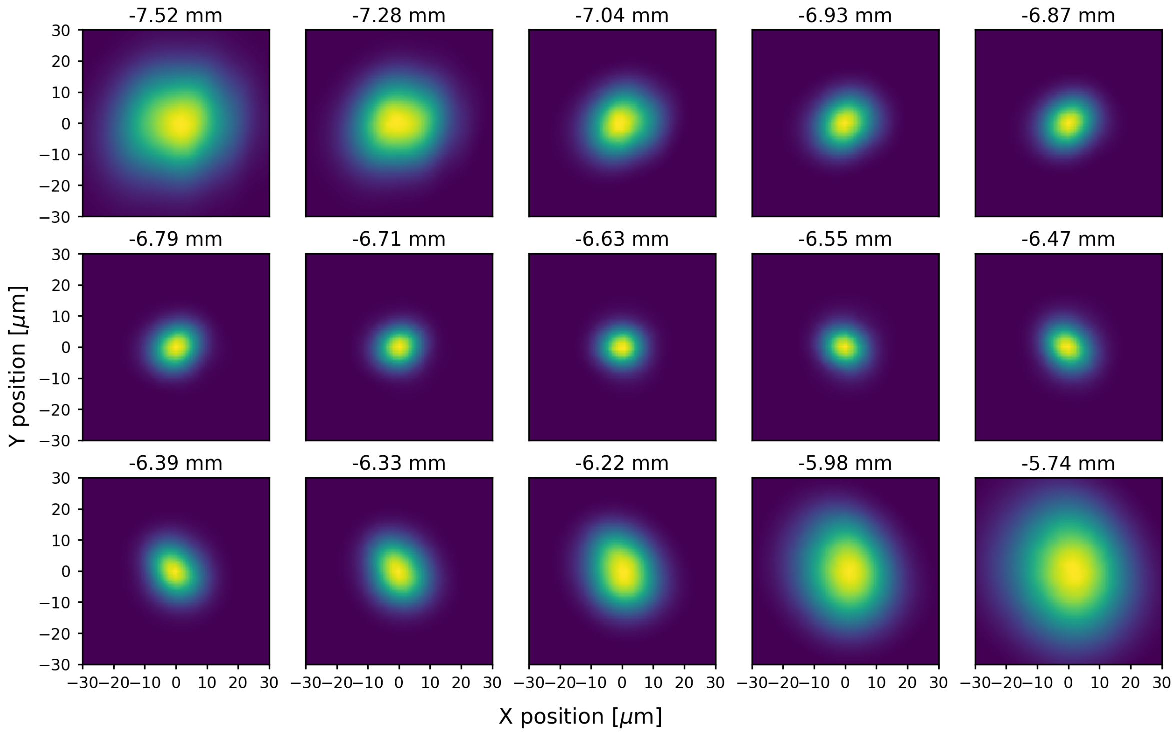

Figure 3.3: Representative reconstructed beam profiles measured at different axial positions using the 100 mm focusing lens.

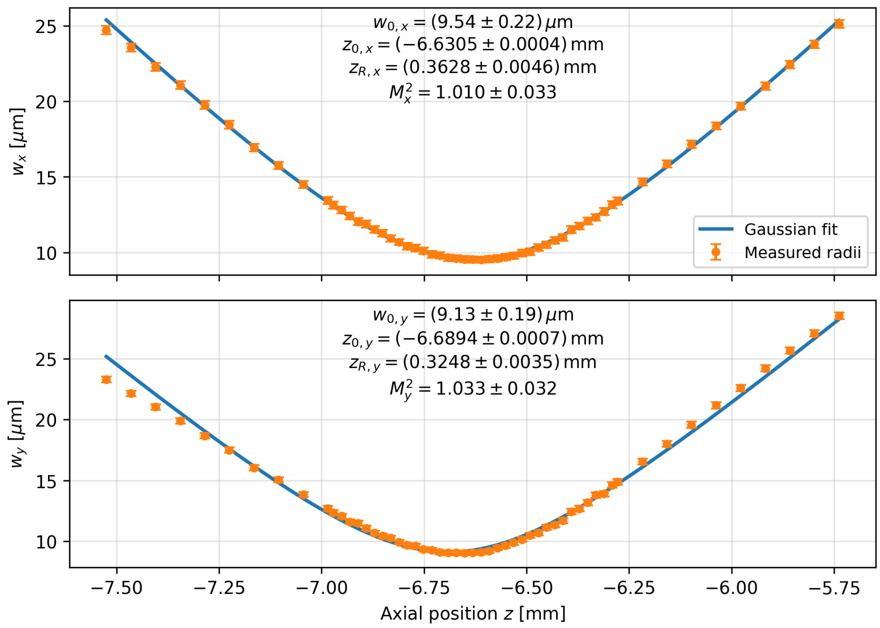

Figure 3.4: Measured beam radii together with the fitted Gaussian beam propagation model for the 100 mm focusing lens.

50 mm focusing lens

The corresponding propagation measurement obtained using the 50 mm focusing lens is shown in Figures 3.5 and 3.6. As expected, the shorter focal length produces a substantially smaller beam waist and a shorter Rayleigh length compared with the 100 mm focusing lens.

Similar to the previous measurement, the reconstructed beam profiles remain well described by Gaussian intensity distributions over the complete propagation range. The beam ellipticity exhibits the same behavior as observed for the 100 mm focusing lens, becoming nearly circular in the vicinity of the beam waist while increasing again on either side of the focus. The corresponding change in the orientation of the major beam axis is again consistent with weak astigmatism of the optical system.

Figure 3.6 shows the measured beam radii together with the fitted Gaussian beam propagation model. The measured beam radii follow the expected propagation behavior and the extracted beam parameters are summarized in Table 3.2.

In contrast to the previous measurement, the fitted beam quality factors are slightly below the physical limit of $M^2 = 1$. Since values below unity are not physically meaningful, this result indicates the presence of residual systematic errors in the measurement or reconstruction procedure rather than an actual improvement of the beam quality.

For the two measurement planes located farthest beyond the beam waist, a small localized reduction in intensity is visible near the beam center. Since this feature appears only for these measurements, it is unlikely to represent a physical property of the laser beam. A possible explanation is an incorrect transition between detector gain settings, leading to a local underestimation of the measured intensity. However, the origin of this artifact cannot be determined from the present measurements alone and should therefore be investigated in future measurements.

The propagation measurements performed using both focusing lenses demonstrate that the developed beam profiler consistently reconstructs the evolution of focused Gaussian beams over a wide range of beam sizes. The expected scaling of the beam waist and Rayleigh length with focal length is reproduced, while the reconstructed beam profiles reveal consistent features such as weak astigmatism in both optical configurations.

At the same time, the measurements also highlight the current limitations of the system. In particular, the unphysical M^2 values obtained for the 50 mm lens and the localized reconstruction artifact observed for the largest beam diameters indicate that further improvements in the calibration and reconstruction procedure are required. These observations provide valuable guidance for future optimization of the beam profiler.

The quantitative accuracy of the extracted beam parameters is investigated in the following section by comparison with a camera-based measurement system.

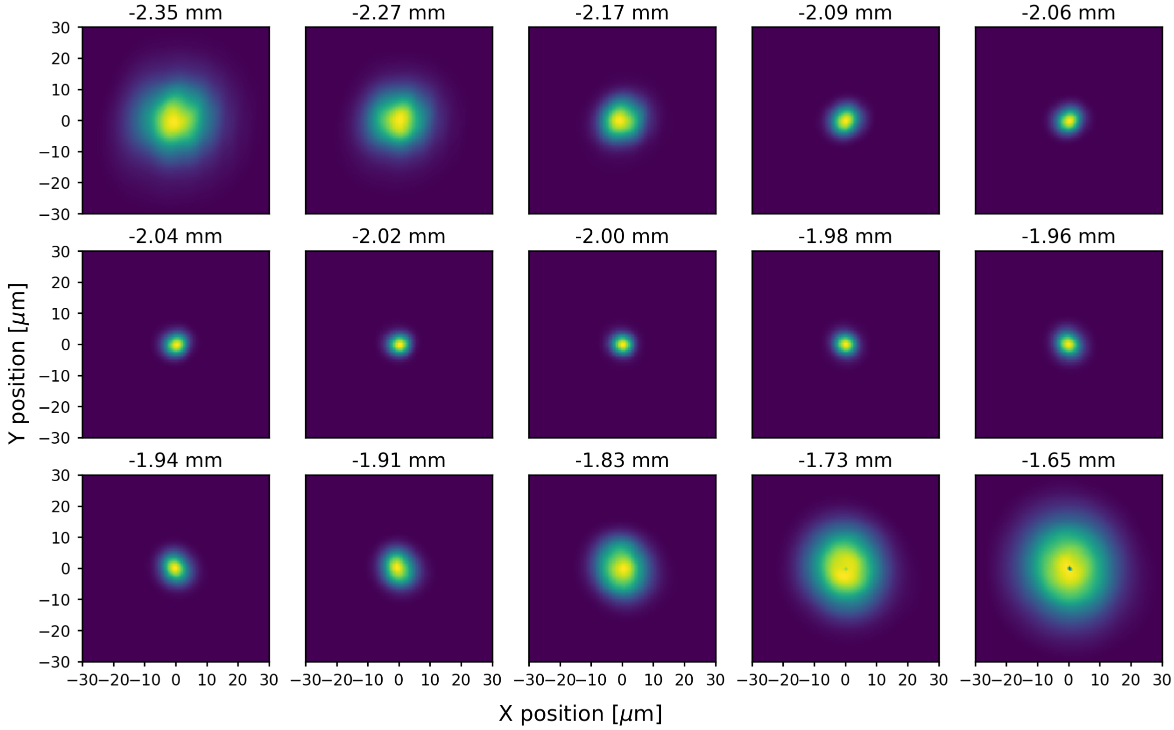

Figure 3.5: Representative reconstructed beam profiles measured at different axial positions using the 50 mm lens.

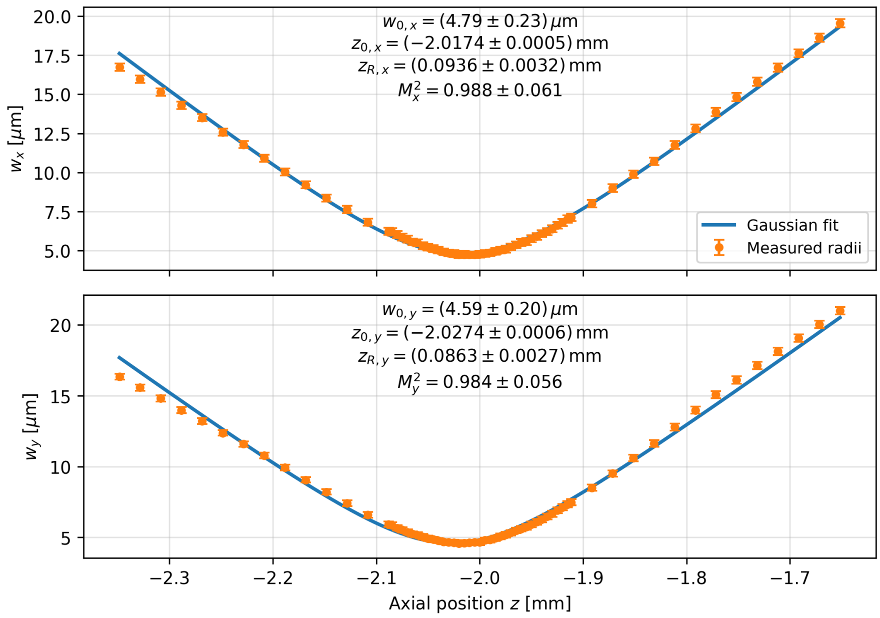

Figure 3.6: Measured beam radii together with the fitted Gaussian beam propagation model for the 50 mm lens.

3.3 Comparison with a camera-based beam profiler

To assess the quantitative accuracy of the developed beam profiler, the beam propagation measurement obtained with the 50 mm focusing lens was repeated using a CCD camera (IDS U3-36P0XCP-M-NO). The camera features a pixel size of 1.4 µm and an optical area of 7168 × 5376 mm. Both measurements were performed under identical optical conditions and analyzed using the same Gaussian beam propagation model introduced in Section 2.4.2. The extracted beam parameters are summarized in Table 3.3, while the measured beam propagation is shown in Figure 3.7.

Although both measurement systems reproduce the overall beam propagation consistently, noticeable differences in the extracted beam waist are observed, which are analyzed in the following.

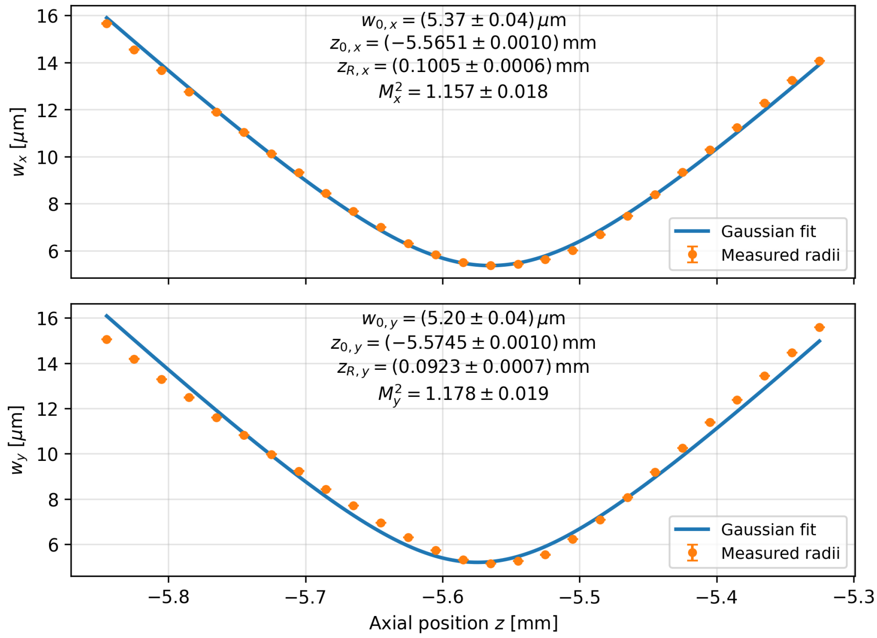

Figure 3.7: Measured beam radii together with the fitted Gaussian beam propagation model for the 50 mm lens.

Parameter	Pinhole profiler	Camera profiler
$w_{0,x}$ [µm]	4.79 ± 0.23	5.37 ± 0.04
$w_{0,y}$ [µm]	4.59 ± 0.20	5.20 ± 0.04
$z_{R,x}$ [mm]	0.0936 ± 0.0032	0.1005 ± 0.0006
$z_{R,y}$ [mm]	0.0863 ± 0.0027	0.0923 ± 0.0007
M_x^2	0.988 ± 0.061	1.157 ± 0.018
M_y^2	0.984 ± 0.056	1.178 ± 0.019

Table 3.3: Comparison of the propagation parameters obtained using the developed beam profiler and the camera-based reference measurement.

A systematic difference is observed in the extracted beam parameters. The beam waist radii obtained with the developed pinhole beam profiler are approximately 11 % smaller in the horizontal direction and 12 % smaller in the vertical direction than those measured with the camera-based profiler. Since the relative deviation is nearly identical in both transverse directions, it suggests a common systematic influence rather than independent axis-specific measurement errors.

The discrepancy is already visible in the reconstructed transverse beam profiles close to the beam waist and is therefore likely to originate from the determination of the individual beam radii rather than from the subsequent beam propagation fit. Since the same Gaussian fitting procedure and propagation model were applied to both data sets, the mathematical model is unlikely to be the dominant source of the observed difference. The good agreement between the measured data and the Gaussian model demonstrates that both the beam shape and its evolution along the propagation direction are reconstructed consistently. However, a good Gaussian fit does not necessarily imply that the absolute spatial scaling of the reconstructed beam profile is correct.

One possible explanation is a systematic error in the spatial calibration of the positioning system. A constant scaling error of the transverse position would preserve the Gaussian beam shape while systematically changing the extracted beam radius. Consequently, excellent agreement between the measured beam profiles and the Gaussian model is compatible with a systematic error in the extracted beam waist. The nearly identical relative deviation observed in both transverse directions is consistent with such an explanation. However, no independent calibration of the positioning system was performed, so this interpretation cannot be verified based on the present measurements alone. Furthermore, the present measurements do not allow potential calibration errors of the transverse and axial positioning axes to be distinguished.

Another possible source of uncertainty is the automatic gain switching of the photodetector. Small discontinuities are visible at the transition between adjacent gain levels in some reconstructed beam profiles, indicating that residual uncertainties in the gain calibration may still be present. Since the gain transition occurs only over a limited intensity range near the beam center, such an error would primarily introduce a local distortion of the intensity profile rather than a uniform scaling of the extracted beam radius. This behaviour appears less consistent with the nearly identical deviation observed in both transverse directions, although its contribution cannot be excluded based on the available measurements.

The finite size of the pinhole aperture is unlikely to explain the observed discrepancy. As discussed in Section 2.6, the finite aperture introduces only a small broadening of the measured beam profile. This effect is considerably smaller than the observed difference and would moreover increase rather than decrease the extracted beam waist.

Further evidence for the presence of a systematic error is provided by the beam quality factors obtained for the 50 mm focusing lens. The measured values are slightly below the physical limit of $M^2 = 1$. Since the beam quality factor depends quadratically on the beam waist radius, an underestimation of the beam waist directly results in a smaller value of M^2. Although the origin of this systematic deviation cannot be identified unambiguously, the obtained values indicate that a remaining systematic error affects the extracted beam parameters.

CHAPTER 4

Conclusion and Outlook

In this bachelor's thesis, an automated pinhole-based beam profiler for the characterization of tightly focused laser beams was developed, implemented, and experimentally evaluated. For this purpose, a 1 µm pinhole was mounted on a motorized three-axis translation stage to scan the laser beam both transversely and along its propagation direction. The transmitted optical power was detected by a photodetector, digitized using the analog-to-digital converter of an Arduino Nano, and processed to reconstruct two-dimensional beam intensity distributions and determine the beam propagation characteristics.

To enable automated and reproducible measurements, automatic beam localization, an adaptive scan strategy, and automatic detector gain adjustment were implemented. In addition, the photodetector was characterized experimentally to determine its linear operating range, gain switching thresholds, and gain factors. A complete data analysis pipeline, including detector calibration, Gaussian fitting, uncertainty propagation, and Gaussian beam propagation analysis, was developed to extract the characteristic beam parameters. Furthermore, the assumptions and limitations of the implemented pinhole measurement principle were investigated analytically and numerically, confirming that aperture-induced broadening remains below 0.5 % for the intended operating range and that diffraction does not significantly affect the extracted beam parameters.

The developed beam profiler was evaluated by measuring the propagation of a 780 nm single-mode laser beam focused by 100 mm and 50 mm lenses. For both configurations, the measured beam profiles were well described by two-dimensional Gaussian functions, and the extracted beam radii were in good agreement with the Gaussian beam propagation model. For the 100 mm lens, beam waists of $w_x = (9.54 \pm 0.05)$ µm and $w_y = (9.07 \pm 0.05)$ µm were obtained, corresponding to beam quality factors of $M_x^2 = 1.01 \pm 0.02$ and $M_y^2 = 1.03 \pm 0.02$. For the 50 mm lens, the measured beam waists were $w_x = (4.79 \pm 0.04)$ µm and $w_y = (4.59 \pm 0.04)$ µm, with corresponding beam quality factors of $M_x^2 = 0.98 \pm 0.03$ and $M_y^2 = 1.01 \pm 0.03$. The measured value of $M_x^2 = 0.98 \pm 0.03$ is physically impossible and therefore indicates the presence of residual systematic uncertainties.

Comparison with the reference measurements performed using a CCD camera mounted on the same translation stage yielded qualitatively consistent beam propagation curves and reproduced the same slight beam ellipticity. However, the CCD camera measurements resulted in systematically larger beam waists of $w_x = (10.59 \pm 0.04)$ µm and $w_y = (10.08 \pm 0.04)$ µm for the 100 mm lens, and $w_x = (5.37 \pm 0.03)$ µm and $w_y = (5.15 \pm 0.03)$ µm for the 50 mm lens. Corresponding beam quality factors between $M^2 = 1.16 \pm 0.01$ and 1.18 ± 0.02 were obtained. While the developed beam profiler reproduced the beam propagation and the observed beam ellipticity, the systematic deviations with respect to the reference measurements indicate that the implemented pinhole-based measurement approach still exhibits residual systematic uncertainties.

Overall, this work establishes a foundation for the automated characterization of tightly focused laser beams using a pinhole-based beam profiler. Although the developed system successfully reconstructs beam profiles and beam propagation, the comparison with the reference CCD camera measurements revealed a systematic underestimation of the beam waist and beam quality factor. Before the profiler can be used for reliable quantitative beam characterization, the origin of these systematic deviations must be identified and eliminated.

Furthermore, additional validation measurements are required to assess the performance of the implemented measurement concept under a wider range of experimental conditions. In particular, the influence of the automatic detector gain adjustment on the reconstructed beam profiles should be investigated to determine whether it contributes to the observed systematic deviations. Finally, the profiler should be evaluated using more tightly focused laser beams approaching the resolution limits of conventional camera-based beam profiling. Such measurements would demonstrate whether the developed pinhole-based beam profiler can accurately characterize beam waists that cannot be reliably resolved using existing beam profiling instruments.

APPENDIX A

Appendix

A.1 Analytical Evaluation of the Finite Pinhole Effect

As discussed in Section 2.6, the detector signal measured by the pinhole beam profiler corresponds to the convolution of the true beam intensity distribution with the circular aperture function. Rather than evaluating the full two-dimensional convolution directly, the following derivation estimates the aperture-induced broadening using the additivity of second central moments under convolution.

Because both the Gaussian beam and the circular aperture are radially symmetric, the aperture-induced broadening can be analyzed independently along either transverse axis. The following derivation therefore considers the one-dimensional second central moment. The resulting beam-radius error is compared in the main text with a full numerical two-dimensional convolution of an ideal Gaussian beam. Assuming the beam is centered at the origin, the second central moment of a one-dimensional intensity distribution is defined as

$$\sigma^2 = \frac{\int_{-\infty}^{\infty} x^2 I(x)\,\mathrm{d}x}{\int_{-\infty}^{\infty} I(x)\,\mathrm{d}x}. \tag{A.1}$$

For an ideal Gaussian beam

$$I(x) = I_0 \exp\left(-\frac{2x^2}{w^2}\right), \tag{A.2}$$

the variance is

$$\sigma_{\mathrm{beam}}^2 = \frac{w^2}{4}, \tag{A.3}$$

where w denotes the $1/e^2$ beam radius.

The pinhole is modeled as an ideal uniform circular aperture with diameter d. Owing to its radial symmetry, the variance of the aperture projected onto either transverse axis is

$$\sigma_{\mathrm{pinhole}}^2 = \frac{d^2}{16}. \tag{A.4}$$

For normalized functions, the second central moments are additive under convolution [12]. The variance of the measured beam profile therefore becomes

$$\sigma_{\text{meas}}^2 = \sigma_{\text{beam}}^2 + \sigma_{\text{pinhole}}^2. \tag{A.5}$$

Substituting the corresponding expressions yields

$$\sigma_{\text{meas}}^2 = \frac{w^2}{4} + \frac{d^2}{16}. \tag{A.6}$$

Expressing the measured variance in terms of the equivalent Gaussian beam radius,

$$\sigma_{\text{meas}} = \frac{w_{\text{meas}}}{2}, \tag{A.7}$$

gives

$$w_{\text{meas}} = \sqrt{w^2 + \frac{d^2}{4}}. \tag{A.8}$$

The relative broadening introduced by the finite aperture is therefore

$$\epsilon = \frac{w_{\text{meas}} - w}{w}, \tag{A.9}$$

which can be written as

$$\boxed{\epsilon\left(\frac{w}{d}\right) = \sqrt{1 + \frac{1}{4\,(w/d)^2}} - 1.} \tag{A.10}$$

The resulting expression depends only on the beam-radius-to-aperture ratio w/d. It therefore provides a convenient analytical estimate of the systematic broadening introduced by the finite aperture. The analytical approximation was validated by comparison with numerical two-dimensional convolution, showing excellent agreement over the investigated range of beam-radius-to-aperture ratios.

Bibliography

[1] C. J. Foot, *Atomic Physics*, Oxford Master Series in Atomic, Optical and Laser Physics, Oxford: Oxford University Press, 2005, ISBN: 9780198506966 (cit. on p. 1).

[2] O. Firstenberg, C. S. Adams and S. Hofferberth, *Nonlinear quantum optics mediated by Rydberg interactions*, Journal of Physics B: Atomic, Molecular and Optical Physics **49** (2016) 152003, URL: `https://doi.org/10.1088/0953-4075/49/15/152003` (cit. on p. 1).

[3] C. B. Roundy and K. D. Kirkham, "Current Technology of Laser Beam Profile Measurements", *Laser Beam Shaping*, ed. by F. M. Dickey, Boca Raton, FL: CRC Press, 2014 463 (cit. on p. 1).

[4] L. G. Cohen, B. E. Little and W. R. Luecke, *Beam-Width Measurement by the Knife-Edge Technique*, Applied Optics (1984) (cit. on p. 1).

[5] Y. Li, E. Lopez, J. Etxebarria-Elezgarai and A. Seifert, *Accurate and Low-Cost Gaussian Beam Profiling with Pinhole and Single-Pixel Detector*, Optics Communications **607** (2026) 132937 (cit. on p. 1).

[6] T. G. Kolda, R. M. Lewis and V. Torczon, *Optimization by Direct Search: New Perspectives on Some Classical and Modern Methods*, SIAM Review **45** (2003) 385 (cit. on p. 6).

[7] W. H. Press et al., *Numerical Recipes: The Art of Scientific Computing*, 3rd ed., Cambridge University Press, 2007, ISBN: 9780521880688 (cit. on p. 6).

[8] J. O. S. III, *Quadratic Interpolation of Spectral Peaks*, CCRMA, Stanford University (1987), Online technical note (cit. on p. 6).

[9] D. Meschede, *Optik, Licht und Laser*, 3rd ed., 2008, ISBN: 978-3-8351-0143-2 (cit. on pp. 10, 11).

[10] T. S. Khwaja and S. A. Reza, *Low-cost Gaussian Beam Profiling with Circular Irises and Apertures*, Applied Optics **58** (2019) 1048 (cit. on p. 11).

[11] A. E. Siegman, "How to (Maybe) Measure Laser Beam Quality", *DPSS (Diode Pumped Solid State) Lasers: Applications and Issues*, vol. 17, OSA Trends in Optics and Photonics, Optical Society of America, 1998 (cit. on p. 12).

[12] J. W. Goodman, *Introduction to Fourier Optics*, 4th ed., W. H. Freeman, 2017 (cit. on pp. 16, 33).

[13] R. N. Bracewell, *The Fourier Transform and Its Applications*, 3rd ed., McGraw-Hill, 2000 (cit. on p. 17).

[14] Q. Cao, *Generalized Jinc Functions and Their Application to Focusing and Diffraction of Circular Apertures*, Journal of the Optical Society of America A **20** (2003) 661 (cit. on p. 18).

[15] M. Born and E. Wolf, *Principles of Optics*, 7th ed., Cambridge University Press, 1999 (cit. on p. 19).

List of Figures

2.1 Schematic overview of the beam profiler. The laser beam is focused onto a pinhole mounted on a motorized translation stage. The transmitted optical power is detected by a photodetector, digitized by an Arduino Nano and processed by the measurement software running on a PC. The photodiode and gain amplifier shown in the figure are integrated in the photodetector. 4

2.2 Flow chart of the implemented beam localization algorithm. Here, $\mathbf{r}_0$ is the initial stage position, h_{i} the current step size along axis i, $S(x_{\mathrm{i}})$ the measured detector signal at position x_{i}, S_{th} the predefined relative threshold, Δ the displacement predicted by the parabolic interpolation and $\mathbf{r}_{\mathrm{w}}$ the estimated beam waist position. 7

2.3 Schematic illustration of the adaptive square spiral scan. Starting from the current scan center, which initially coincides with the localized beam waist, the pinhole is translated along a square spiral trajectory with constant step size h. After each completed spiral ring, the maximum detector signal within the current ring is evaluated. The scan terminates after two consecutive rings whose maximum signal falls below the predefined stopping threshold. The red square indicates the current scan center. 9

2.4 Measured detector output voltage as a function of optical power. The dashed blue line represents the weighted orthogonal distance regression performed within the linear operating range. The dashed red line indicates the upper limit of the linear operating region adopted for the automatic gain adjustment. The inset shows the onset of detector saturation at high optical powers. 13

2.5 Experimentally determined voltage amplification factors for the individual 10 dB gain steps. The dashed line indicates the ideal amplification factor of $10^{10/20} \approx 3.16$. Error bars represent the propagated uncertainties of the measured amplification factors. . . . 15

2.6 Experimentally determined cumulative effective detector gain relative to the nominal gain settings. The dashed line indicates the ideal detector gain. 16

2.7 Illustration of aperture-induced broadening for a Gaussian beam with $w/d = 0.75$. The example is intentionally chosen to emphasize the convolution effect and does not represent the operating conditions of the beam profiler. 17

2.8 Relative beam-radius error for an ideal Gaussian beam caused by aperture convolution as a function of the beam-radius-to-aperture ratio w/d. The numerical results closely follow the analytical prediction over the investigated range. 18

3.1 Reconstructed beam profile measured close to the beam waist using a 100 mm focusing lens. The left panel shows the normalized two-dimensional intensity distribution. The right and bottom panels display the corresponding vertical and horizontal cross sections through the fitted beam center. The solid lines represent the fitted Gaussian model. . . 21
3.2 Reconstructed beam profile measured close to the beam waist using a 50 mm focusing lens. The left panel shows the normalized two-dimensional intensity distribution. The right and bottom panels display the corresponding vertical and horizontal cross sections through the fitted beam center. The solid lines represent the fitted Gaussian model. . . 22
3.3 Representative reconstructed beam profiles measured at different axial positions using the 100 mm focusing lens. . . . 25
3.4 Measured beam radii together with the fitted Gaussian beam propagation model for the 100 mm focusing lens. . . . 25
3.5 Representative reconstructed beam profiles measured at different axial positions using the 50 mm lens. . . . 27
3.6 Measured beam radii together with the fitted Gaussian beam propagation model for the 50 mm lens. . . . 27
3.7 Measured beam radii together with the fitted Gaussian beam propagation model for the 50 mm lens. . . . 28

List of Tables

2.1 Experimentally determined effective detector gain relative to the nominal gain settings. 15
2.2 Representative values of the relative beam-radius error caused by aperture convolution for different beam-radius-to-aperture ratios. Analytical and numerical results are listed for comparison. 18

3.1 Measurement parameters used for the transverse beam-profile measurements. 20
3.2 Beam propagation parameters obtained from the Gaussian beam fits. 24
3.3 Comparison of the propagation parameters obtained using the developed beam profiler and the camera-based reference measurement. 28

Used tools

The following tools were used during the preparation of this bachelor's thesis:

- **ChatGPT (OpenAI)** was used for language improvement of the manuscript, primarily to improve clarity, grammar, spelling, and overall readability. It was also used as a programming assistant during software development, particularly for implementing the communication and control of the motorized translation stage and the Arduino Nano, as well as supporting the implementation of the automated measurement procedure.
- **Python** was used for measurement automation, data acquisition, data analysis, numerical simulations, and the generation of several figures.
- **Inkscape** was used for the creation of figures included in this thesis.